SCIENCE CHINA
Information Sciences

• RESEARCH PAPER •

November 2016, Vol. 59 112211:1–112211:16
doi: 10.1007/s11432-014-0838-7

Simplified ultra-tightly coupled BDS/INS integrated navigation system

Kanghua TANG*, Bing LUO & Xiaofeng HE

College of Mechatronics and Automation, National University of Defense Technology, Changsha 410073*, China*

Received June 10, 2016; accepted July 13, 2016; published online October 10, 2016

Abstract Due to advantages such as low cost, small size, low weight, low power consumption, powerful capability of anti-jamming, and high dynamics, ultra-tightly coupled GNSS/MIMU integrated navigation systems are extensively used in projectile and precision-guided munitions. To overcome the nonlinearity of baseband signal processing and the complexity of the navigation filter, in this paper, we design a novel architecture for the ultra-tightly coupled (UTC) Beidou navigation satellite system (BDS)/INS integration based on the BDS B3 signal, including the combination of code phase and carrier phase dynamics baseband prefilter model, and the navigation filter navigation error propagation and measurement models. To eliminate the clock state components, i.e., the receiver clock offset and clock drift, the pseudorange, delta pseudorange, and delta pseudorange rate residuals obtained from baseband signal prefilters are differenced between two satellites. Based on the BDS/INS simulator, a test system for the UTC BDS/INS integrated navigation system is developed and UTC performance is evaluated. Some preliminary conclusions are formed about the effectiveness of the UTC BDS/INS integration approach.

Keywords BDS/INS ultra-tightly coupled integrated navigation system, baseband signal preprocessing, high dynamics, BDS/INS simulator

Citation Tang K H, Luo B, He X F. Simplified ultra-tightly coupled BDS/INS integrated navigation system. Sci China Inf Sci, 2016, 59(11): 112211, doi: 10.1007/s11432-014-0838-7

1 Introduction

Global navigation satellite system (GNSS)/inertial navigation system (INS) integrated navigation systems provide a high-quality and reliable solution for high-rate maneuvering platforms such as missiles, precision-guided munitions (PGMs), unmanned air vehicles (UAVs), and aircrafts. GNSS/INS integrated navigation systems also provide a good and reliable solution for the interference problem. The complexity and cost of integrated systems are generally acceptable for manned aircrafts, missiles, and UAVs that carry both systems. The integrated system becomes necessary for missile systems, PGMs, and projectiles to handle the extreme dynamics, rapidly changing GNSS visibility, and jamming [1].

Based on different data fusion strategies, GNSS/INS integrated systems can be divided into three types: loosely coupled GNSS/INS, tightly coupled GNSS/INS, and ultra-tightly coupled GNSS/INS [1, 2].

The most commonly implemented integration scheme is called the loosely coupled approach wherein the GNSS-derived positions and velocities, and their accuracies obtained from the GNSS Kalman filter

* Corresponding author (email: tt_kanghua@hotmail.com)

(KF) are used as measurements for the GNSS/INS integrated navigation KF. The error states include both the navigation errors and sensor errors. To further improve the accuracy of the navigation solution, the error states are fed back to the inertial navigation algorithm. A tightly coupled GNSS/INS integrated navigation system uses the GNSS pseudorange and pseudorange rate as measurements for the GNSS/INS integrated navigation KF. The last integration architecture is the ultra-tightly coupled (UTC) GNSS/INS integrated navigation system [2–5].

The UTC integration method combines the GNSS/INS integrated navigation and GNSS signal tracking process into a single information fusion algorithm. It uses the in-phases (Is) and quadraphases (Qs) from the GNSS correlators as measurements for the integration KF. The numerically controlled oscillator (NCO) is controlled by the value estimated by the integration KF, to decrease GNSS signal tracking errors and enhance the GNSS receiver positioning, dynamics, and anti-jamming performance, in addition to helping the receiver tracking loop to retrieve signal lock if it is lost due to interference or jamming [2].

Generally, the UTC integrated navigation system can be classified as either centralized or cascaded architecture. In the centralized architecture, only a centralized filter is used to estimate the navigation and sensor errors. Using Is and Qs from the GNSS correlation channels as measurements of the navigation filter (NF), a complex relationship between Is/Qs measurements and INS error states has to be established [6–10].

The centralized architecture has the following drawbacks:

(1) Use of Is and Qs from the GNSS correlation channels as measurements of the navigation filter can greatly increase the processing load for the algorithm implementation, because of the high rate of Is/Qs measurements update (for GPS C/A code, Is/Qs update rate is 1 kHz).

(2) Because there are no direct relationships between baseband measurements Is/Qs and error states of the navigation filter, the measurement model is highly nonlinear.

(3) Is/Qs measurements are directly related to the polarity of GNSS navigation data messages, so the GNSS navigation data bit must be determined before the navigation filter.

In the cascaded architecture, based on the vector-based tracking structure of GNSS receiver [11, 12], two cascades of filters are adopted. The code tracking and carrier tracking are performed in a filter, usually called the baseband signal pre-processing filter or prefilter (PF), and the navigation filter is used to process the output of the PFs and to restrict the INS errors [13]. The cascaded architecture enables the application of the UTC GNSS/INS integrated navigation for highly dynamic platforms [5, 13–17].

Compared with the centralized UTC GNSS/INS integration architecture, the cascaded architecture has the following advantages:

(1) PFs can provide the output to NF at a slower rate, so that NF can update at a low rate (such as 1 Hz) and requires a lower processing capacity.

(2) Due to the use of baseband prefilters, real-time processing of the GNSS receiver baseband signal and the knowledge of the GNSS navigation data bit are not necessary.

(3) The measurement model of the navigation filter is simple and easy to implement.

The current cascaded architecture also exhibits the following problems:

(1) Due to the high nonlinearity in baseband signal processing, many researchers [5, 14–17] adopted the simplified linear processing method, decreasing the precision of the method.

(2) Due to the nonlinearity in baseband signal processing and the complexity of the navigation filter, a nonlinear filter method is used to improve the performance of the UTC GNSS/INS integration. However, the implementation of this algorithm is quite challenging. Therefore, it is necessary to develop a method that can simultaneously consider the complexity and the performance of the algorithm. Our contributions to the UTC GNSS/INS integration are as follows:

(1) We present a novel cascaded architecture for the UTC Beidou (or COMPASS) navigation satellite system (BDS)/INS integration based on the combination of code phase and carrier phase dynamics baseband prefilter model.

(2) To eliminate the clock state components, i.e., the receiver clock offset and clock drift, the pseudorange, delta pseudorange, and delta pseudorange rate residuals are differenced between two satellites.

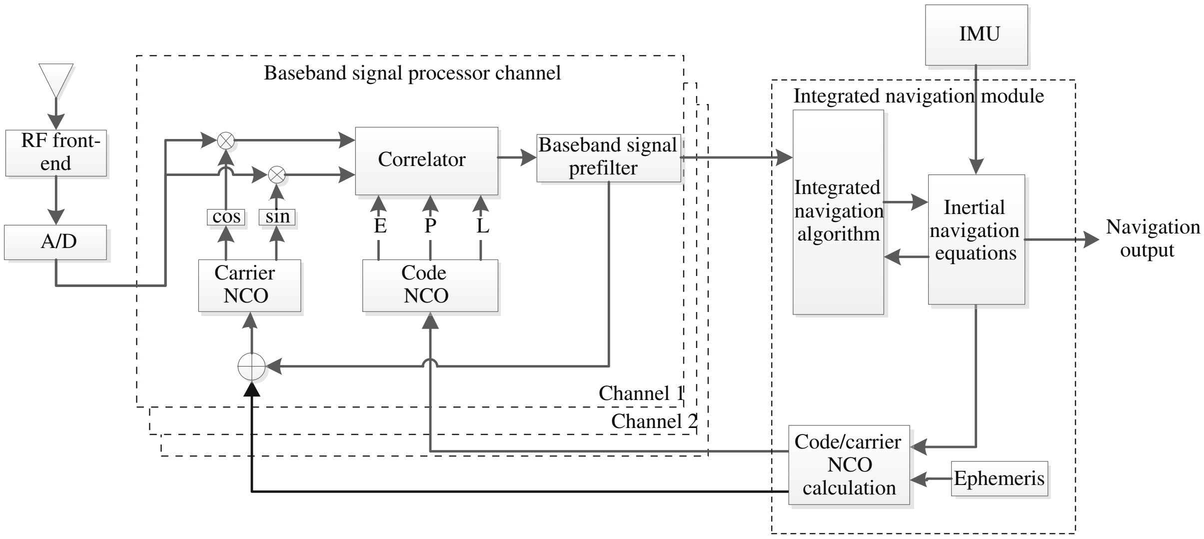

Figure 1 The structure of ultra-tightly coupled BDS/INS integrated navigation system.

Therefore, the reduced-dimension KF structure is adopted for the BDS/INS navigation filter in order to improve the performance of the BDS/INS navigation filter.

(3) We then test the proposed UTC BDS/INS integration. Based on the BDS/INS simulator, a test system for the UTC BDS/INS integrated navigation system is developed, and the dynamic and tracking sensitivity performances of the UTC BDS/INS integration are tested.

This paper is organized as follows. Section 1 describes the design of the novel cascaded architecture of the UTC Beidou (or COMPASS) navigation satellite system (BDS)/INS integration, which includes the combination of code phase and carrier phase dynamics baseband prefilter model. Section 2 describes the design of the navigation filter navigation error propagation model and the navigation filter measurement models. In Section 3, to eliminate the clock state components, i.e., the receiver clock offset and clock drift, the pseudorange, delta pseudorange, and delta pseudorange rate residuals are differenced between two satellites. Section 4 describes the development of a test system for the UTC BDS/INS integrated navigation system based on the BDS/INS simulator and presents the experimental results. Section 5 concludes the paper.

2 Combination of code phase and carrier phase dynamics baseband pre-filter model

The key features of the ultra-tightly coupled BDS/INS integrated navigation system are illustrated in Figure 1. As in a conventional BDS receiver, the first stage in each channel is in-phase and quadraphase sampling, also known as carrier wipe-off or Doppler wipe-off. The pseudorandom noise (PRN) codes for each satellite are then correlated with the internally generated replica codes. After an integrate-and-dump operation in the correlator shown in Figure 1, the outputs of the receiver correlator consist of a set of accumulated in-phase and quadraphase signals. These traditional receiver components are shown to the left of the dashed line in Figure 1.

In UTC BDS/INS integration structure, the solution is to break up KFs into cascaded filters for each satellite. Fast tracking filters for each satellite, known as prefilters, estimate the code-phase, carrier-phase, and carrier-frequency tracking errors and provide pseudorange and pseudorange rate or delta range measurement innovations to a centralized NF as output. Depending on the navigation-data-message rate, the PFs typically perform measurement updates at 500 Hz for the BDS B3 signal, transforming and compressing the data into a slower rate. The slow NF typically performs measurement updates at 10 Hz, estimating a number of system error states that are used to correct the INS, the inertial measurement unit (IMU), and the BDS receiver clock. The corrected INS position and velocity together with satellite ephemeris data are transformed to line-of-sight coordinates and are used to construct pseudorange and delta range estimates for feedback to the NCOs in the BDS receiver.

The designed KF error models for the prefilter are described as follows.

Using in-phase and quadraphase signal components of the BDS receiver baseband signal, the PFs output the error residuals, representing, among others, the code phase error (pseudorange error) and the change in carrier phase error over a time interval (delta range error). These measurements, including the corresponding measurement noise matrices, are passed to the centralized NF, which performs the processing to correct the INS, the IMU, and the BDS receiver clock. The most commonly used methods of baseband signal preprocessing include the least-squares curve fitting method [18–20] and the K method [21–23].

The prefilter states are defined as

$$\boldsymbol{X}_k = \left[\, t_k \;\; \varphi_k \;\; \Delta f_k \;\; \Delta \dot{f}_k \,\right]^{\mathrm{T}}, \tag{1}$$

where t_k is the code phase error (chips), φ_k is the carrier phase error (rad/2π), Δf_k is the carrier frequency error (Hz), and $\Delta \dot{f}_k$ is the carrier phase acceleration (Hz/s).

The combination of code phase and carrier phase dynamics baseband prefilter model takes the form of a discrete-time triple integrator driven by a discrete-time white noise described as follows:

$$\begin{bmatrix} t_{k+1} \\ \varphi_{k+1} \\ \Delta f_{k+1} \\ \Delta \dot{f}_{k+1} \end{bmatrix} = \begin{bmatrix} 1 & 0 & \frac{f_{\mathrm{co}}}{f_{\mathrm{ca}}}\tau & 0 \\ 0 & 1 & \tau & \tau^2/2 \\ 0 & 0 & 1 & \tau \\ 0 & 0 & 0 & 1 \end{bmatrix} \begin{bmatrix} t_k \\ \varphi_k \\ \Delta f_k \\ \Delta \dot{f}_k \end{bmatrix} + \begin{bmatrix} 1 & 0 & 0 & 0 \\ 0 & 1 & 0 & 0 \\ 0 & 0 & 1 & 0 \\ 0 & 0 & 0 & 1 \end{bmatrix} \begin{bmatrix} w_{\mathrm{co}} \\ w_{\mathrm{ca}} \\ w_f \\ w_a \end{bmatrix}, \tag{2}$$

where f_{co} is the code chipping rate for the BDS B3 CA code, $f_{\mathrm{co}} = 10.23$ MHz, f_{ca} is the carrier frequency for BDS B3, $f_{\mathrm{ca}} = 1268.52$ MHz, τ is the PF update period for BDS B3, $\tau = 1$ ms, w_{co} represents the code phase noise due to the clock bias, w_{ca} represents the carrier phase noise due to the clock bias, w_f represents the carrier frequency noise due to the clock drift, and w_a represents the carrier phase acceleration noise due to the BDS receiver dynamics. The system noise is defined as a Gaussian white noise sequence with a covariance matrix Q_k.

The measurements are outputs of code and carrier discriminators, and the corresponding measurement model is given by

$$Z_k = \begin{bmatrix} t_k \\ \varphi_k \end{bmatrix} = \begin{bmatrix} \frac{\sqrt{I_E^2+Q_E^2}-\sqrt{I_L^2+Q_L^2}}{\sqrt{I_E^2+Q_E^2}+\sqrt{I_L^2+Q_L^2}} \\ \frac{a\tan(Q_p/I_p)}{2\pi} \end{bmatrix} + \boldsymbol{V}_k, \tag{3}$$

where I_E, I_p, and I_L are the early, prompt, and late in-phase accumulated correlator outputs, respectively, Q_E, Q_p, and Q_L are the early, prompt, and late quadraphase accumulated correlator outputs, respectively, and $\boldsymbol{V}_k = [\, v_1 \;\; v_2 \,]^{\mathrm{T}}$, v_1 and v_2 are the output noise of the code and carrier discriminators, respectively. The measurements noise is defined as a Gaussian white noise sequence with a covariance matrix R_k.

The measurements vector Z_k is related to the state vector X_k via the measurement matrix $\boldsymbol{H}_k$,

$$\boldsymbol{H}_k = \begin{bmatrix} 1 & 0 & 0 & 0 \\ 0 & 1 & 0 & 0 \end{bmatrix}, \tag{4}$$

so that

$$Z_k = \begin{bmatrix} 1 & 0 & 0 & 0 \\ 0 & 1 & 0 & 0 \end{bmatrix} \begin{bmatrix} t_k \\ \varphi_k \\ \Delta f_k \\ \Delta \dot{f}_k \end{bmatrix} + \boldsymbol{V}_k = \boldsymbol{H}_k \boldsymbol{X}_k + \boldsymbol{V}_k. \tag{5}$$

3 Navigation filter model

3.1 Navigation error propagation model

The navigation error propagation equation for a strapdown inertial navigation system can be derived for different types of coordinate frames. We consider the error propagation equation for the Earth-centered Earth-fixed (ECEF) coordinate frame, because GNSS produces position and velocity output in the ECEF frame.

The errors in the estimates of position, velocity, attitude, and deviations in the inertial sensors from their ideal values are considered in the error propagation equations. At the same time, the GNSS receiver clock offset, the GNSS receiver clock drift and the clock g-dependent error coefficients are considered in the error propagation equations. The state vector therefore becomes

$$\boldsymbol{X} = \left[(\boldsymbol{\delta R}^e)^{\mathrm{T}}, (\boldsymbol{\delta V}^e)^{\mathrm{T}}, (\boldsymbol{\varepsilon}^e)^{\mathrm{T}}, \left(\boldsymbol{\delta\omega^b}\right)^{\mathrm{T}}, \left(\boldsymbol{\delta a}^b\right)^{\mathrm{T}}, \delta b, \delta d, (S_{cg})^{\mathrm{T}}\right]^{\mathrm{T}}, \tag{6}$$

where $\boldsymbol{\delta R}^e = [\delta R_x, \delta R_y, \delta R_z]^{\mathrm{T}}$ is the positional error in the ECEF frame, $\boldsymbol{\delta V}^e = [\delta V_x, \delta V_y, \delta V_z]^{\mathrm{T}}$ is the velocity error in the ECEF frame, $\boldsymbol{\varepsilon}^e$ is the attitude error, $\boldsymbol{\delta\omega}^b$ is the gyro bias, $\boldsymbol{\delta a}^b$ is the accelerometer bias, δb is the GNSS receiver clock offset, δd is the GNSS receiver clock drift, and $S_{cg} = [s_{cgx}, s_{cgy}, s_{cgz}]^{\mathrm{T}}$ are the clock g-dependent error coefficients, where it is assumed that the axes of the receiver's reference oscillator are fixed with respect to the IMU.

Based on the work of reference [2], the linear error propagation equations for the ECEF frame is described as follows:

$$\dot{\boldsymbol{X}}(t) = \begin{bmatrix} \boldsymbol{\delta\dot{R}}^e \\ \boldsymbol{\delta\dot{V}}^e \\ \dot{\boldsymbol{\varepsilon}}^e \\ \boldsymbol{\delta\dot{\omega}}^b \\ \boldsymbol{\delta\dot{a}}^b \\ \delta\dot{b} \\ \delta\dot{d} \\ \dot{S}_{cg} \end{bmatrix} = \begin{bmatrix} \boldsymbol{\delta V}^e \\ -\boldsymbol{F}^e\boldsymbol{\varepsilon} + \boldsymbol{C}_b^e\boldsymbol{\delta a}^b - 2\boldsymbol{\Omega}_{ie}^e\boldsymbol{\delta V}^e + \boldsymbol{N}^e\boldsymbol{\delta R}^e \\ -\boldsymbol{\Omega}_{ie}^e\boldsymbol{\varepsilon}^e + \boldsymbol{C_b^e}\boldsymbol{\delta\omega}^b \\ \boldsymbol{W}_\omega \\ \boldsymbol{W}_a \\ \delta d + \hat{f}_{ib}^b S_{cg} \\ w_{d\rho} \\ 0 \end{bmatrix}, \tag{7}$$

where $\boldsymbol{C}_b^e$ is the directional cosine matrix from the vehicle body fixed coordinate frame (B-frame) to the ECEF frame, $\boldsymbol{W}_\omega$ is the gyro random noise with power spectral densities n_{rg}^2, $\boldsymbol{W}_a$ is the accelerometer random noise with power spectral densities n_{ra}^2, $w_{d\rho}$ is the random walk of the receiver clock drift with power spectral densities n_{bgd}^2, and $\hat{f}_{ib}^b = [\hat{f}_{ibx}^b, \hat{f}_{iby}^b, \hat{f}_{ibz}^b]$ is the specific force measured by the IMU.

In (7),

$$\boldsymbol{N}^e = \frac{GM}{r^3}\begin{bmatrix} -1+\frac{3x^3}{r^2} & \frac{3xy}{r^2} & \frac{3xz}{r^2} \\ \frac{3xy}{r^2} & -1+\frac{3y^3}{r^2} & \frac{3yz}{r^2} \\ \frac{3xz}{r^2} & \frac{3yz}{r^2} & -1+\frac{3z^3}{r^2} \end{bmatrix} + \begin{bmatrix} \omega_e^2 & 0 & 0 \\ 0 & \omega_e^2 & 0 \\ 0 & 0 & 0 \end{bmatrix}, \tag{8}$$

$$\boldsymbol{F}^e = \begin{bmatrix} 0 & f_z & -f_y \\ -f_z & 0 & f_x \\ f_y & -f_x & 0 \end{bmatrix}, \tag{9}$$

$$\boldsymbol{\Omega}_{ie}^e = \begin{bmatrix} 0 & \omega_e & 0 \\ -\omega_e & 0 & 0 \\ 0 & 0 & 0 \end{bmatrix}, \tag{10}$$

where $r = \sqrt{x^2+y^2+z^2}$, GM are the Earth's gravitational constant and their WGS84 value is $3.986004418 \times 10^{14}$ $\mathrm{m^3/s^2}$, $\omega_e = 7.292115 \times 10^{-5}$ rad/s is the Earth's angular rate, $\boldsymbol{R}^e = (x, y, z)$ is the position in the ECEF frame, and $[\, f_x \;\; f_y \;\; f_z \,]$ is the specific force in the ECEF frame.

3.2 Measurement models

UTC BDS/INS integration uses the BDS receiver baseband processor's pseudorange and pseudorange-rate measurements that are obtained from the baseband signal prefilter. The measurement innovation vector comprises the differences between the BDS measured pseudorange and pseudorange rates and the values predicted from the corrected inertial navigation solution at the same time of validity; the differences between estimated receiver clock offset and drift and the navigation-data-indicated satellite positions and velocities.

For n tracked satellites, the pseudorange ρ^j of the jth satellite is given by

$$\rho^j = \left[\left(x - x_s^j\right)^2 + \left(y - y_s^j\right)^2 + \left(y - y_s^j\right)^2\right]^{\frac{1}{2}} + \delta b, \tag{11}$$

where $j = 1, 2, \ldots, n$, (x_s^j, y_s^j, z_s^j) is the position of the jth satellite, (x, y, z) is the position of the BDS receiver, and δb is the BDS receiver clock offset.

Eq. (11) is linearized by performing a Taylor expansion about a predicted user position and clock offset as follows:

$$\delta\rho^j = -\boldsymbol{e}^j \boldsymbol{\delta R}^e + \hat{b} - b = -\boldsymbol{e}^j \boldsymbol{\delta R}^e + \delta b + \nu_\rho^j, \tag{12}$$

where $\boldsymbol{\delta R}^e$ is the receiver position error vector in the ECEF frame and ν_ρ^j is the measurement residual. The line-of-sight vector from the jth satellite to the receiver is

$$\boldsymbol{e}^j = \frac{1}{\rho_0^j}\left[\left(x_s^j - x\right), \left(y_s^j - y\right), \left(z_s^j - z\right)\right], \tag{13}$$

where $\rho_0 = [(x - x_s^j)^2 + (y - y_s^j)^2 + (y - y_s^j)^2]^{\frac{1}{2}}$.

For n tracked satellites, we let

$$\boldsymbol{\delta\rho} = \begin{pmatrix} \delta\rho^1 \\ \delta\rho^2 \\ \vdots \\ \delta\rho^n \end{pmatrix}, \quad \boldsymbol{U} = \begin{pmatrix} \boldsymbol{e}^1 \\ \boldsymbol{e}^2 \\ \vdots \\ \boldsymbol{e}^n \end{pmatrix}, \quad \boldsymbol{\nu_\rho} = \begin{pmatrix} \nu_\rho^1 \\ \nu_\rho^2 \\ \vdots \\ \nu_\rho^n \end{pmatrix}. \tag{14}$$

Eq. (12) is then replaced by

$$\boldsymbol{\delta\rho} = -\boldsymbol{U}\boldsymbol{\delta R}^e + \boldsymbol{1_n}\delta b + \boldsymbol{\nu_\rho}, \tag{15}$$

where $\boldsymbol{1}_n = (1, 1, \ldots, 1)^{\mathrm{T}}$.

For the BDS receiver, the Doppler-shift measurement is obtained directly from the carrier tracking loop. This may be transformed to a pseudorange-rate measurement. For the jth satellite, the accumulated delta range is the integral of the pseudorange rate:

$$\Delta\rho^j = \int_{t_1}^{t_2} \dot{\rho}^j \mathrm{d}t = \rho_2^j - \rho_1^j, \tag{16}$$

where ρ_2^j and ρ_1^j are the jth satellite pseudo-range for time t_2 and t_1, respectively.

The jth satellite's difference between the accumulated delta range $\Delta\hat{\rho}^j$ predicted from the corrected inertial navigation solution, and the accumulated delta range $\Delta\rho^j$ measured by the BDS receiver is defined as follows:

$$\Delta\hat{\rho}^j - \Delta\rho^j = \hat{\rho}_2^j - \rho_2^j - (\hat{\rho}_1^j - \rho_1^j). \tag{17}$$

From (12), the jth satellite's difference is then as follows:

$$\Delta\hat{\rho}^j - \Delta\rho^j = -\boldsymbol{e^j}(t_2)\boldsymbol{\delta R^e}(t_2) + \delta b(t_2) + \boldsymbol{e^j}(t_1)\boldsymbol{\delta R^e}(t_1) - \delta b(t_1) + \nu_{\Delta\rho}^j, \tag{18}$$

where $\nu_{\Delta\rho}^j$ is the accumulated delta range residual.

The BDS receiver position error vector $\boldsymbol{\delta R}^e$ and the BDS receiver clock offset δb can often be approximated by the following equation:

$$\begin{aligned}&\boldsymbol{\delta R}^e(t_1)=\boldsymbol{\delta R}^e(t_2)-\Delta t\cdot\boldsymbol{\delta V}^e(t_2)-\tfrac{1}{2}\Delta t^2\cdot\boldsymbol{\delta a}^e(t_2),\\&\delta b(t_1)=\delta b(t_2)-\Delta t\cdot\delta d(t_2),\end{aligned}\tag{19}$$

where $\boldsymbol{\delta a}^e$ is the acceleration error in the ECEF frame, δd is the receiver clock offset, t_2 is the current time, t_1 is the previous time, and $\Delta t=t_2-t_1$.

Substituting (19) into (18), we obtain the following equation:

$$\begin{aligned}\Delta\hat{\rho}^j-\Delta\rho^j\;=&-\left[\boldsymbol{e}^j(t_2)-\boldsymbol{e}^j(t_1)\right]\cdot\boldsymbol{\delta R}^e(t_2)-\Delta t\cdot\boldsymbol{e}^j(t_1)\cdot\boldsymbol{\delta V}^e(t_2)\\&-\frac{1}{2}\Delta t^2\cdot\boldsymbol{e}^j(t_1)\cdot\boldsymbol{\delta a}^e(t_2)+\Delta t\cdot\delta d(t_2)+\nu^j_{\Delta\rho}.\end{aligned}\tag{20}$$

From (7), $\boldsymbol{\delta a}^e$ can be approximated as follows:

$$\boldsymbol{\delta a}^e=\boldsymbol{C}^e_b\boldsymbol{\delta a}^b-\boldsymbol{F}^e\boldsymbol{\varepsilon}^e.\tag{21}$$

Substituting (21) into (20), we obtain the following equation:

$$\Delta\hat{\rho}^j-\Delta\rho^j=-\boldsymbol{\Delta e}^j\cdot\boldsymbol{\delta R}^e-\Delta t\cdot\boldsymbol{e}^j_1\cdot\boldsymbol{\delta V}^e-\frac{1}{2}\Delta t^2\cdot\boldsymbol{e}^j_1\cdot\boldsymbol{C}^e_b\cdot\boldsymbol{\delta a}^b+\frac{1}{2}\Delta t^2\cdot\boldsymbol{e}^j_1\cdot\boldsymbol{F}^e\cdot\boldsymbol{\varepsilon}^e+\Delta t\cdot\delta d+\nu^j_{\Delta\rho},\tag{22}$$

where $\boldsymbol{\Delta e}^j=\boldsymbol{e}^j(t_2)-\boldsymbol{e}^j(t_1)$ and $\boldsymbol{e}^j_1=\boldsymbol{e}^j(t_1)$.

Let n be the number of satellites that are tracked, and let

$$\boldsymbol{\delta\Delta\rho}=\begin{pmatrix}\Delta\hat{\rho}^1-\Delta\rho^1\\\Delta\hat{\rho}^2-\Delta\rho^2\\\vdots\\\Delta\hat{\rho}^n-\Delta\rho^n\end{pmatrix},\quad\boldsymbol{\Delta U}=\begin{pmatrix}\boldsymbol{\Delta e}^1\\\boldsymbol{\Delta e}^2\\\vdots\\\boldsymbol{\Delta e}^n\end{pmatrix},\quad\boldsymbol{U}_1=\begin{pmatrix}\boldsymbol{e}^1_1\\\boldsymbol{e}^2_1\\\vdots\\\boldsymbol{e}^n_1\end{pmatrix},\quad\boldsymbol{\nu_{\Delta\rho}}=\begin{pmatrix}\nu^1_{\Delta\rho}\\\nu^2_{\Delta\rho}\\\vdots\\\nu^n_{\Delta\rho}\end{pmatrix}.\tag{23}$$

Then

$$\boldsymbol{\delta\Delta\rho}=-\boldsymbol{\Delta U}\cdot\boldsymbol{\delta R}^e-\Delta t\cdot\boldsymbol{U}_1\cdot\boldsymbol{\delta V}^e-\frac{1}{2}\Delta t^2\cdot\boldsymbol{U}_1\cdot\boldsymbol{C}^e_b\cdot\boldsymbol{\delta a}^b+\frac{1}{2}\Delta t^2\cdot\boldsymbol{U}_1\cdot\boldsymbol{F}^e\cdot\boldsymbol{\varepsilon}^e+\Delta t\cdot\boldsymbol{1}_n\cdot\delta d+\boldsymbol{\nu_{\Delta\rho}}.\tag{24}$$

Similar to the method for calculation of $\boldsymbol{\delta\Delta\rho}$, $\boldsymbol{\delta\Delta\dot{\rho}}$ can be expressed as follows:

$$\boldsymbol{\delta\Delta\dot{\rho}}=-\boldsymbol{\Delta U}\cdot\boldsymbol{\delta V}^e-\Delta t\cdot\boldsymbol{U}_1\cdot\boldsymbol{F}^e\cdot\boldsymbol{\varepsilon}^e+\Delta t\cdot\boldsymbol{U}_1\cdot\boldsymbol{C}^e_b\cdot\boldsymbol{\delta a}^b+\boldsymbol{\nu_{\Delta\dot{\rho}}},\tag{25}$$

where $\boldsymbol{\nu_{\Delta\dot{\rho}}}$ is the delta range rate noise.

Based on (15), (24), and (25), the vector of measurements $Z_{\rm nav}$ is related to the state vector X as follows:

$$\boldsymbol{Z}_{\rm nav}=\begin{bmatrix}\boldsymbol{F}_1&\boldsymbol{0}&\boldsymbol{0}&\boldsymbol{0}&\boldsymbol{0}&1&0&\boldsymbol{0}\\\boldsymbol{F_2}&\boldsymbol{F_3}&\boldsymbol{F_4}&\boldsymbol{0}&\boldsymbol{F_5}&0&\Delta t&\boldsymbol{0}\\\boldsymbol{0}&\boldsymbol{F}_6&\boldsymbol{F}_7&\boldsymbol{0}&\boldsymbol{F}_8&0&0&\boldsymbol{0}\end{bmatrix}\begin{bmatrix}\boldsymbol{\delta R}^e\\\boldsymbol{\delta V}^e\\\boldsymbol{\varepsilon}^e\\\boldsymbol{\delta\omega}^b\\\boldsymbol{\delta a}^b\\\delta b\\\delta d\\S_{cg}\end{bmatrix}+\begin{bmatrix}\boldsymbol{\nu_\rho}\\\boldsymbol{\nu_{\Delta\rho}}\\\boldsymbol{\nu_{\Delta\dot{\rho}}}\end{bmatrix},\tag{26}$$

where $\boldsymbol{F}_1=-\boldsymbol{U}$, $\boldsymbol{F}_2=-\boldsymbol{\Delta U}$, $\boldsymbol{F_3}=-\Delta t\cdot\boldsymbol{U}_1$, $\boldsymbol{F_4}=\frac{1}{2}\Delta t^2\cdot\boldsymbol{U}_1\cdot\boldsymbol{F}^e$, $\boldsymbol{F_5}=-\frac{1}{2}\Delta t^2\cdot\boldsymbol{U}_1\cdot\boldsymbol{C}^e_b$, $\boldsymbol{F}_6=\boldsymbol{F}_2$, $\boldsymbol{F_7}=-\Delta t\cdot\boldsymbol{U}_1\cdot\boldsymbol{F}^e$, $\boldsymbol{F}_8=\Delta t\cdot\boldsymbol{U}_1\cdot\boldsymbol{C}^e_b$, and $\boldsymbol{0}$ is the 3×3 zero matrix.

The covariance matrix of the navigation filter measurement noise, R_N, is directly related to the covariance matrix of the PF states, P. The P matrix contains correlations among the PF states t_k, φ_k, Δf_k, and $\Delta \dot{f}_k$. Rather than using the fully correlated P matrix to estimate R_N, an approximate representation is used that is suitable for sequential update processing of the navigation filter measurements [13].

For the jth satellite, the variance $\boldsymbol{P}^j$ of the pseudorange can be written as follows [13]:

$$E\left(\nu_\rho^j \cdot \nu_\rho^j\right) = k_1^2 E\left(t_k^j \cdot t_k^j\right) = k_1^2 \boldsymbol{P}_{11}^j, \tag{27}$$

where $k_1 = \lambda_{\mathrm{co}}$, $\lambda_{\mathrm{co}} \approx 29.3$ m is the chip length of the BDS CA code and $\boldsymbol{P}_{11}^j$ is the diagonal element of the prefilter covariance matrix $\boldsymbol{P}^j$ corresponding to $X_1 = t$.

For the delta range $\delta\Delta p$,

$$E\left(\nu_{\Delta\rho}^j \cdot \nu_{\Delta\rho}^j\right) = k_2^2 E\left[(\varphi - \varphi_{\mathrm{old}})^2\right] = k_2^2 E\left[\varphi^2 - 2\varphi\varphi_{\mathrm{old}} + \varphi_{\mathrm{old}}^2\right], \tag{28}$$

where $k_2 = \lambda_{\mathrm{ca}}$, $\lambda_{\mathrm{ca}} \approx 0.236$ m is the wavelength of the BDS B3 carrier. We now assume that $\varphi = \varphi_{\mathrm{old}} + \Delta f_{\mathrm{old}} \Delta t + \frac{1}{2}\Delta \dot{f}_{\mathrm{old}} \Delta t^2$ and substitute for $\varphi\varphi_{\mathrm{old}}$ in (28) to obtain:

$$E\left(\nu_{\Delta\rho}^j \cdot \nu_{\Delta\rho}^j\right) = k_2^2 \left[\boldsymbol{P}_{22}^j - \left(\boldsymbol{P}_{22}^j\right)_{\mathrm{old}} - 2\Delta t \left(\boldsymbol{P}_{23}^j\right)_{\mathrm{old}} - \Delta t^2 \left(\boldsymbol{P}_{24}^j\right)_{\mathrm{old}}\right], \tag{29}$$

where $(\boldsymbol{P}_{ik}^j)_{\mathrm{old}}$ denotes the value of the covariance matrix element at the previous update.

For the delta range rate $\delta\Delta\dot{p}$, let $\Delta f = \Delta f_{\mathrm{old}} + \Delta \dot{f}_{\mathrm{old}} \Delta t$, so that we have the following equation:

$$E\left(\nu_{\Delta\dot{\rho}}^j \cdot \nu_{\Delta\dot{\rho}}^j\right) = k_2^2 \left[\boldsymbol{P}_{33}^j - \left(\boldsymbol{P}_{33}^j\right)_{\mathrm{old}} - 2\Delta t \left(\boldsymbol{P}_{34}^j\right)_{\mathrm{old}}\right]. \tag{30}$$

The navigation filter processes measurements from n prefilters, where n is the number satellite channels in the receiver. Three measurements are used for each prefilter, corresponding to the pseudorange δp^j, delta pseudorange $\Delta\delta p^j$, and delta pseudorange rate $\Delta\delta\dot{p}^j$ residuals. These are obtained from the prefilter states as follows:

$$\boldsymbol{Z}^j = \begin{bmatrix} \delta p^j \\ \Delta\delta p^j \\ \Delta\delta\dot{p}^j \end{bmatrix} = \begin{bmatrix} t_k^j \cdot \lambda_{\mathrm{co}} \\ \left(\varphi_k^j - \varphi_{k-1}^j\right) \cdot \lambda_{\mathrm{ca}} \\ \left(\Delta f_k^j - \Delta f_{k-1}^j\right) \cdot \lambda_{\mathrm{ca}} \end{bmatrix}, \tag{31}$$

where$j$ denotes the jth tracked satellite. The $3n$ measurements are generated at every prefilter update, at a rate of 500 Hz, corresponding to 2 ms navigation-data-message rate of the BDS B3 signal. However, the navigation filter accepts this data at a much slower rate, typically at 10 Hz.

4 Reduced-dimension navigation filter

In a typical UTC GNSS/INS integrated navigation system, the state vector of the navigation filter includes data such as the receiver clock offset and clock drift. To eliminate the clock state components, i.e., the receiver clock offset and clock drift, the pseudorange, delta pseudorange, and delta pseudorange rate residuals are differenced between two satellites. Therefore, the NF state vector is modified as follows:

$$\boldsymbol{X} = \left[(\boldsymbol{\delta R}^e)^{\mathrm{T}}, (\boldsymbol{\delta V}^e)^{\mathrm{T}}, (\boldsymbol{\varepsilon}^e)^{\mathrm{T}}, (\boldsymbol{\delta\omega}^b)^{\mathrm{T}}, (\boldsymbol{\delta a}^b)^{\mathrm{T}}\right]^{\mathrm{T}}, \tag{32}$$

and the error dynamics are given by the following equation:

$$\dot{\boldsymbol{X}}(t) = \begin{bmatrix} \boldsymbol{\delta\dot{R}}^e \\ \boldsymbol{\delta\dot{V}}^e \\ \dot{\boldsymbol{\varepsilon}}^e \\ \boldsymbol{\delta\dot{\omega}}^b \\ \boldsymbol{\delta\dot{a}}^b \end{bmatrix} = \begin{bmatrix} \boldsymbol{0}_{3\times3} & \boldsymbol{I}_{3\times3} & \boldsymbol{0}_{3\times3} & \boldsymbol{0}_{3\times3} & \boldsymbol{0}_{3\times3} \\ \boldsymbol{N}^e & -2\boldsymbol{\Omega}_{ie}^e & -\boldsymbol{F}^e & \boldsymbol{0}_{3\times3} & \boldsymbol{C}_b^e \\ \boldsymbol{0}_{3\times3} & \boldsymbol{0}_{3\times3} & -\boldsymbol{\Omega}_{ie}^e & \boldsymbol{C}_b^e & \boldsymbol{0}_{3\times3} \\ \boldsymbol{0}_{3\times3} & \boldsymbol{0}_{3\times3} & \boldsymbol{0}_{3\times3} & \boldsymbol{0}_{3\times3} & \boldsymbol{0}_{3\times3} \\ \boldsymbol{0}_{3\times3} & \boldsymbol{0}_{3\times3} & \boldsymbol{0}_{3\times3} & \boldsymbol{0}_{3\times3} & \boldsymbol{0}_{3\times3} \end{bmatrix} \begin{bmatrix} \boldsymbol{\delta R}^e \\ \boldsymbol{\delta V}^e \\ \boldsymbol{\varepsilon}^e \\ \boldsymbol{\delta\omega}^b \\ \boldsymbol{\delta a}^b \end{bmatrix} + \begin{bmatrix} \boldsymbol{0}_{3\times3} & \boldsymbol{0}_{3\times3} \\ \boldsymbol{0}_{3\times3} & \boldsymbol{0}_{3\times3} \\ \boldsymbol{0}_{3\times3} & \boldsymbol{0}_{3\times3} \\ \boldsymbol{I}_{3\times3} & \boldsymbol{0}_{3\times3} \\ \boldsymbol{0}_{3\times3} & \boldsymbol{I}_{3\times3} \end{bmatrix} \begin{bmatrix} \boldsymbol{W}_\omega \\ \boldsymbol{W}_a \end{bmatrix}, \tag{33}$$

where $\mathbf{0}_{3\times3}$ and $\boldsymbol{I}_{3\times3}$ are the 3×3 null and identity matrices, respectively.

Using (15), the single difference BDS pseudorange residual between the ith satellite and the jth satellite can be expressed by the following equation:

$$\delta\rho^{ij} = -\boldsymbol{e}^{ij}\boldsymbol{\delta R}^e + \nu_\rho^{ij}, \tag{34}$$

where the ith satellite is the reference satellite and $j = 1, 2, \ldots, n,\ j \neq i$.

For the all tracked satellites, the single difference pseudorange residual can be described as follows:

$$\nabla\boldsymbol{\delta\rho} = -\nabla\boldsymbol{U}\cdot\boldsymbol{\delta R}^e + \boldsymbol{\nu}_{\nabla\boldsymbol{\rho}}, \tag{35}$$

where

$$\nabla\boldsymbol{\delta\rho} = \begin{pmatrix} \delta\rho^1 - \delta\rho^i \\ \delta\rho^2 - \delta\rho^i \\ \vdots \\ \delta\rho^n - \delta\rho^i \end{pmatrix}_{n-1}, \quad \nabla\boldsymbol{U} = \begin{pmatrix} \boldsymbol{e}^1 - \boldsymbol{e}^i \\ \boldsymbol{e}^2 - \boldsymbol{e}^i \\ \vdots \\ \boldsymbol{e}^n - \boldsymbol{e}^i \end{pmatrix}_{n-1}, \quad \boldsymbol{\nu}_{\nabla\boldsymbol{\rho}} = \begin{pmatrix} \nu_\rho^1 - \nu_\rho^i \\ \nu_\rho^2 - \nu_\rho^i \\ \vdots \\ \nu_\rho^n - \nu_\rho^i \end{pmatrix}_{n-1}. \tag{36}$$

Based on (24) and using the ith satellite as the reference satellite, the single difference delta pseudorange residual measurement is given by the following equation:

$$\nabla\delta\Delta\rho^{ij} = -\boldsymbol{\Delta e}^{ij}\cdot\boldsymbol{\delta R}^e - \Delta t\cdot\boldsymbol{e}_1^{ij}\cdot\boldsymbol{\delta V}^e - \frac{1}{2}\Delta t^2\cdot\boldsymbol{e}_1^{ij}\cdot\boldsymbol{C}_b^e\cdot\boldsymbol{\delta a}^b + \frac{1}{2}\Delta t^2\cdot\boldsymbol{e}_1^{ij}\cdot\boldsymbol{F}^e\cdot\boldsymbol{\varepsilon}^e + \nu_{\Delta\rho}^{ij}. \tag{37}$$

For the all tracked satellites, Eq. (37) can be rewritten as follows:

$$\nabla\boldsymbol{\delta\Delta\rho} = -\nabla\boldsymbol{\Delta U}\cdot\boldsymbol{\delta R}^e - \Delta t\cdot\nabla\boldsymbol{U}_1\cdot\boldsymbol{\delta V}^e - \frac{1}{2}\Delta t^2\cdot\nabla\boldsymbol{U}_1\cdot\boldsymbol{C}_b^e\cdot\boldsymbol{\delta a}^b + \frac{1}{2}\Delta t^2\cdot\nabla\boldsymbol{U}_1\cdot\boldsymbol{F}^e\cdot\boldsymbol{\varepsilon}^e + \boldsymbol{\nu}_{\nabla\boldsymbol{\Delta\rho}}, \tag{38}$$

where

$$\begin{gathered} \nabla\boldsymbol{\delta\Delta\rho} = \begin{pmatrix} \delta\Delta\rho^1 - \delta\Delta\rho^i \\ \delta\Delta\rho^2 - \delta\Delta\rho^i \\ \vdots \\ \delta\Delta\rho^n - \delta\Delta\rho^i \end{pmatrix}_{n-1}, \quad \nabla\boldsymbol{\Delta U} = \begin{pmatrix} \boldsymbol{\Delta e}^1 - \boldsymbol{\Delta e}^i \\ \boldsymbol{\Delta e}^2 - \boldsymbol{\Delta e}^i \\ \vdots \\ \boldsymbol{\Delta e}^n - \boldsymbol{\Delta e}^i \end{pmatrix}_{n-1}, \\ \nabla\boldsymbol{U}_1 = \begin{pmatrix} \boldsymbol{e}_1^1 - \boldsymbol{e}_1^i \\ \boldsymbol{e}_1^2 - \boldsymbol{e}_1^i \\ \vdots \\ \boldsymbol{e}_1^n - \boldsymbol{e}_1^i \end{pmatrix}_{n-1}, \quad \boldsymbol{\nu}_{\nabla\boldsymbol{\Delta\rho}} = \begin{pmatrix} \nu_{\Delta\rho}^1 - \nu_{\Delta\rho}^i \\ \nu_{\Delta\rho}^2 - \nu_{\Delta\rho}^i \\ \vdots \\ \nu_{\Delta\rho}^n - \nu_{\Delta\rho}^i \end{pmatrix}_{n-1}. \end{gathered} \tag{39}$$

Because the measurement of delta pseudorange rate residual is independent of the receiver clock offset and clock drift, evaluation of the difference is unnecessary. Thus,

$$\boldsymbol{\delta\Delta\dot\rho} = -\boldsymbol{\Delta U}\cdot\boldsymbol{\delta V}^e - \Delta t\cdot\boldsymbol{U}_1\cdot\boldsymbol{F}^e\cdot\boldsymbol{\varepsilon}^e + \Delta t\cdot\boldsymbol{U}_1\cdot\boldsymbol{C}_b^e\cdot\boldsymbol{\delta a}^b + \boldsymbol{\nu}_{\boldsymbol{\Delta\dot\rho}}. \tag{40}$$

Based on (35), (38), and (40), the vector of measurements is related to the state vector as follows:

$$\begin{bmatrix} \nabla\boldsymbol{\delta\rho} \\ \nabla\boldsymbol{\delta\Delta\rho} \\ \boldsymbol{\delta\Delta\dot\rho} \end{bmatrix} = \begin{bmatrix} -\boldsymbol{\Delta U} & \mathbf{0} & \mathbf{0} & \mathbf{0} & \mathbf{0} \\ -\nabla\boldsymbol{\Delta U} & \boldsymbol{A1} & \boldsymbol{A}2 & \mathbf{0} & \boldsymbol{A}3 \\ \mathbf{0} & -\boldsymbol{\Delta U} & \boldsymbol{A}4 & \mathbf{0} & \boldsymbol{A}5 \end{bmatrix} \begin{bmatrix} \boldsymbol{\delta R}^e \\ \boldsymbol{\delta V}^e \\ \boldsymbol{\varepsilon} \\ \boldsymbol{\delta\omega}^b \\ \boldsymbol{\delta a}^b \end{bmatrix} + \begin{bmatrix} \boldsymbol{\nu}_{\nabla\boldsymbol{\rho}} \\ \boldsymbol{\nu}_{\nabla\boldsymbol{\Delta\rho}} \\ \boldsymbol{\nu}_{\boldsymbol{\Delta\dot\rho}} \end{bmatrix}, \tag{41}$$

where $\boldsymbol{A1} = -\Delta t\cdot\nabla\boldsymbol{U}_1$, $\boldsymbol{A}2 = \frac{1}{2}\cdot\Delta t^2\cdot\nabla\boldsymbol{U}_1\cdot\boldsymbol{F}^e$, $\boldsymbol{A}3 = -\frac{1}{2}\Delta t^2\cdot\nabla\boldsymbol{U}_1\cdot\boldsymbol{C}_b^e$, $\boldsymbol{A}4 = -\Delta t\cdot\boldsymbol{U}_1\cdot\boldsymbol{F}^e$, and $\boldsymbol{A}5 = \Delta t\cdot\boldsymbol{U}_1\cdot\boldsymbol{C}_b^e$.

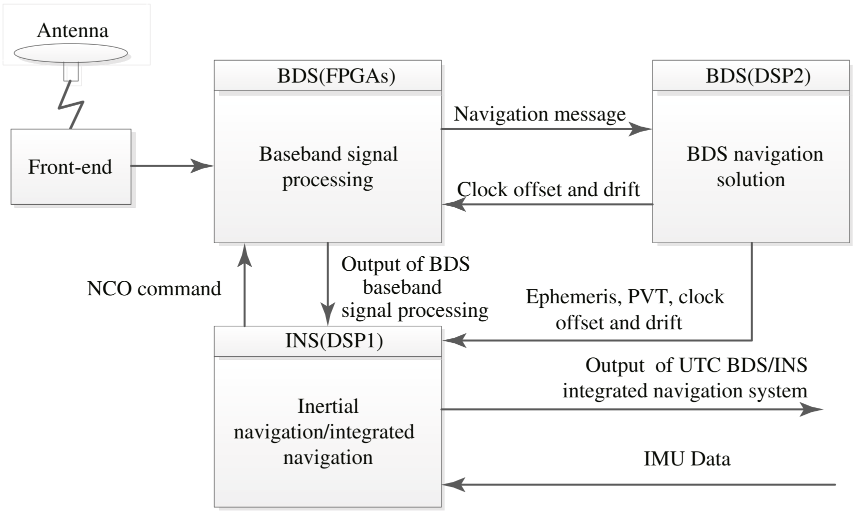

Figure 2 Architecture of the UTC BDS/INS integrated navigation system.

Based on (27) and considering that each satellite tracked measurement noise is uncorrelated, the variance of the single difference pseudorange residual can be expressed as follows:

$$E\left(\nu_{\rho}^{ij}\cdot\nu_{\rho}^{ij}\right)=k_1^2E\left(\left(\nu_{\rho}^{j}-\nu_{\rho}^{i}\right)\cdot\left(\nu_{\rho}^{j}-\nu_{\rho}^{i}\right)\right)=k_1^2\left(\boldsymbol{P}_{11}^{j}+\boldsymbol{P}_{11}^{i}\right). \tag{42}$$

Similarly, the variance of the single difference delta pseudorange residual can be expressed as follows:

$$\begin{aligned}E\left(\nu_{\Delta\rho}^{ij}\cdot\nu_{\Delta\rho}^{ij}\right) &= k_2^2E\left[\left(\nu_{\Delta\rho}^{j}-\nu_{\Delta\rho}^{i}\right)\cdot\left(\nu_{\Delta\rho}^{j}-\nu_{\Delta\rho}^{i}\right)\right]\\ &= k_2^2\Big[\boldsymbol{P}_{22}^{j}-\left(\boldsymbol{P}_{22}^{j}\right)_{\text{old}}-2\Delta t\left(\boldsymbol{P}_{23}^{j}\right)_{\text{old}}-\Delta t^2\left(\boldsymbol{P}_{24}^{j}\right)_{\text{old}}\\ &\quad+\boldsymbol{P}_{22}^{i}-\left(\boldsymbol{P}_{22}^{i}\right)_{\text{old}}-2\Delta t\left(\boldsymbol{P}_{23}^{i}\right)_{\text{old}}-\Delta t^2\left(\boldsymbol{P}_{24}^{i}\right)_{\text{old}}\Big].\end{aligned} \tag{43}$$

The expression for the variance of the delta pseudorange rate residual can be found in (30).

5 Results and discussion

5.1 System architecture overview

To evaluate the performance of the proposed UTC BDS/INS integration method, the UTC BDS/INS integrated navigation system was designed. The UTC system architecture is shown in Figure 2.

As shown in Figure 2, the signal processor of the UTC system is highly integrated and composed of the BDS receiver RF frontend, a FPGA signal processor that supports BDS baseband signal processing, a DSP processor that incorporates the electronics and software to host BDS PVT functions and another DSP processor that supports inertial navigation, BDS/INS integrated navigation, and NCO command generation functions. This highly integrated design approach results in improved performance as well as a low cost design and manufacturing process. In the absence of inertial navigation data input to the signal processor, the UTC BDS/INS integrated navigation system can operate in the BDS receiver mode. The UTC BDS/INS integrated navigation system is shown in Figure 3.

5.2 Experimental test description

To verify the performance of the proposed UTC BDS/MIMU system using the BDS/INS simulator produced by National University of Defense Technology, a test system was constructed as shown in Figure 4.

The BDS/INS simulator can generate a simulated BDS B3 RF signal and synchronized IMU data, including gyro and accelerometer data. An arbitrary trajectory can be loaded into the control computer

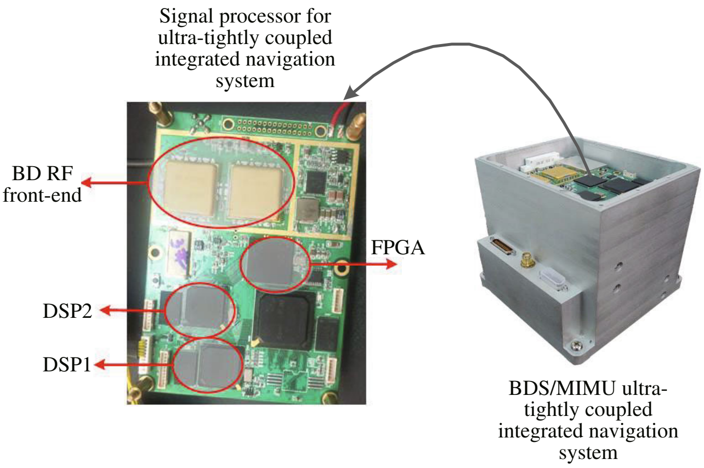

Figure 3 (Color online) Designed UTC BDS/INS integrated navigation system.

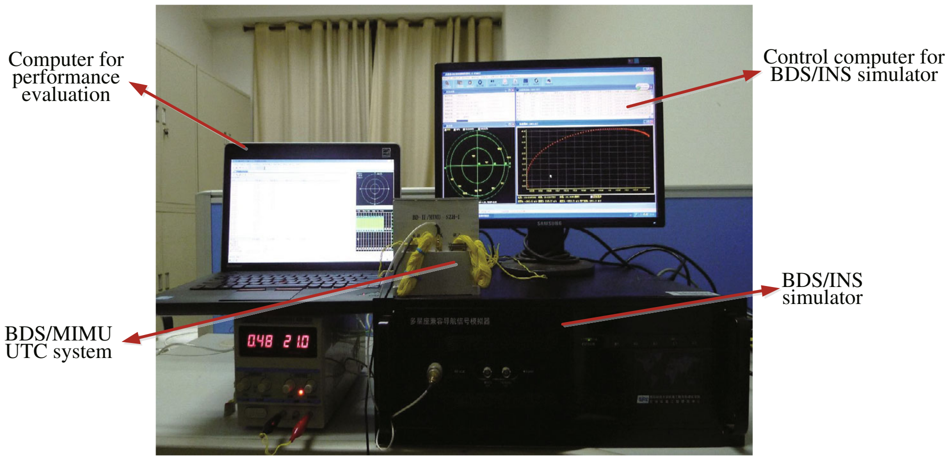

Figure 4 (Color online) Experimental test system for UTC BDS/INS integration.

to drive the BDS/INS simulator. The UTC BDS/INS integrated navigation system processes the BDS B3 RF signal and IMU data using information fusion and generates position, velocity, and attitude solution, usually together with other parameters. The computer used for performance evaluation receives results of UTC BDS/INS integration and reference trajectory of the BDS/INS simulator to evaluate the performance of the UTC BDS/INS integrated navigation system.

5.3 Experimental results

Based on the actual experimental test system, the following six high-dynamics profiles were constructed:

(1) Vertical circle trajectory with maximal acceleration of 50 g and maximal jerk of 5 g/s dynamic conditions.

(2) Vertical circle trajectory with maximal acceleration of 100 g and maximal jerk of 10 g/s dynamic conditions.

(3) Level circle trajectory with maximal acceleration of 50 g and maximal jerk of 5 g/s dynamic conditions.

(4) Level circle trajectory with maximal acceleration of 100 g and maximal jerk of 10 g/s dynamic conditions.

(5) Line-Sine trajectory with maximal acceleration of 50 g and maximal jerk of 5 g/s dynamic conditions.

(6) Line-Sine trajectory with maximal acceleration of 100 g and maximal jerk of 10 g/s dynamic conditions.

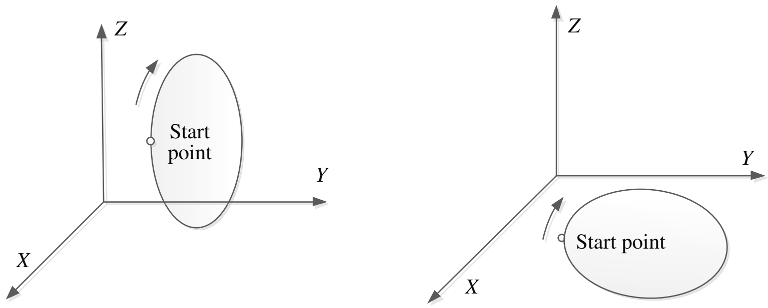

Figure 5 Vertical and level circle test trajectory.

Table 1 Description of level uniform circular motion

Time	1–300 s	301–1800 s
Description of trajectory	Static	Level uniform circular motion: R = 50 km, $\omega = 0.1$ rad/s maximal acceleration of 50 g, maximal jerk of 5 g/s, R = 100 km, $\omega = 0.1$ rad/s maximal acceleration of 100 g, maximal jerk of 10 g/s.

Table 2 MIMU specifications

	MEMS Gyro (1σ)	MEMS Accelerometer (1σ)
Bias	$\leqslant 20°$/h	$\leqslant 1$ mg
Scale factor	200 ppm	100 ppm
Random walk	$\leqslant 0.1°/\sqrt{h}$	$\leqslant 0.01$ m/s/$\sqrt{h}$
Noise	0.005°/s	1 mg

Table 3 Results of position and velocity precision (signal power: −133 dBmW)

	Work mode	Position error (m) (95%)	Velocity error (m/s) (95%)
50 g level circle	BDS receiver	0.66	0.14
	UTC BDS/INS	0.54	0.15
50 g vertical circle	BDS receiver	0.92	0.14
	UTC BDS/INS	0.52	0.14
50 g line-sine	BDS receiver	0.87	0.15
	UTC BDS/INS	0.58	0.14

All designed profiles comprised 300 s of stationary profiles and 1500 s of high dynamic profiles. Figure 5 shows the vertical circle and level circle trajectories.

In Figure 5, the X-Y-Z frame is a local navigation frame. In the level circle trajectory profile, the initial position is as follows: latitude is 112.9916° N, longitude is 28.2203° E, and height is 101 m. The initial velocity is 0 m/s. The initial acceleration is 0 m/s^2 and simulated time is 1800 s. Level uniform circular motion is described in Table 1.

To avoid sudden change of motion's parameters, the circle radius R and angular velocity ω are designed as follows:

$$R = R_0 * (1 - \mathrm{e}^{-t/\tau}), \quad \omega = 0.1 * (1 - \mathrm{e}^{-t/\tau}),$$

where $R_0 = 100000$ for maximal acceleration of 100 g and maximal jerk of 10 g/s, and $R_0 = 50000$ for maximal acceleration of 50 g and maximal jerk of 5 g/s, and $\tau = 50$.

Based on circular motion, angular rate and acceleration can be obtained. Using the gravity model and the earth-rotation angular rate, IMU output, including specific force and angular rate, can be obtained. The simulated MIMU including gyro and accelerometer data are specified in Table 2.

(1) High dynamic test. Based on the high dynamic profiles, the dynamic performance of the UTC BDS/INS integration was tested using the BDS/INS simulator.

The results for 50 g acceleration and 5 g/s jerk dynamic conditions are shown in Table 3.

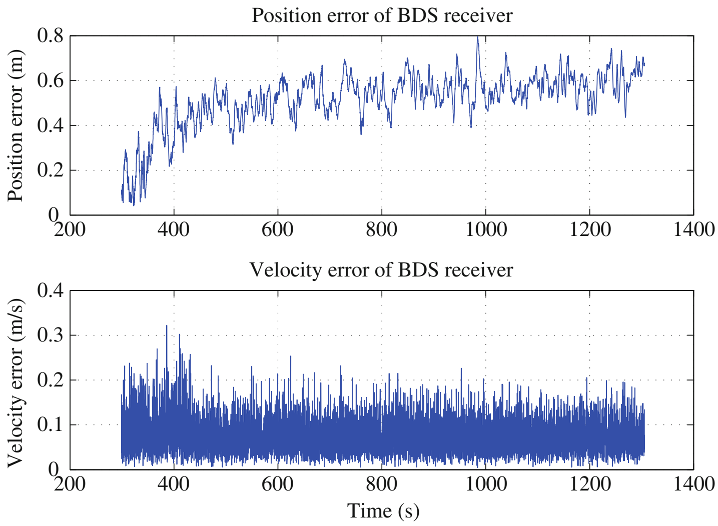

Figure 6 (Color online) Position/velocity error curve of the BDS receiver for 50 g level circle trajectory.

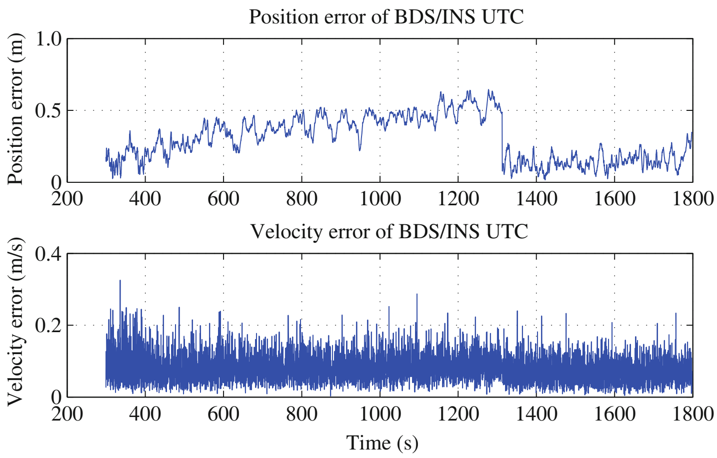

Figure 7 (Color online) Position/velocity error curve of the UTC BDS/INS integration for 50 g level circle trajectory.

Examination of the data in Table 3 for the conditions of 50 g acceleration and 5 g/s jerk high dynamics shows that the designed high-dynamics BDS receiver and the UTC BDS/INS integrated navigation system work well, with the UTC integration improving the precision of obtained positions such that position accuracy can reach about 5.0 m (2σ) and velocity accuracy can reach about 0.2 m/s (2σ). The designed BDS receiver and the UTC BDS/INS integration position/velocity error curves for the level circle trajectory for dynamic conditions with maximal acceleration of 50 g and maximal jerk of 5 g/s using the BDS/INS simulator are shown in Figures 6 and 7, respectively. At the same time, the UTC BDS/INS integration attitude error curves for 50 g level circle trajectory are shown in Figure 8.

The results of the test for the 100 g acceleration and 10 g/s jerk dynamic conditions are shown in Table 4.

Examination of the data in Table 4 for the conditions of 100 g acceleration and 10 g/s jerk high dynamics shows that while the BDS receiver exhibits loss of lock, the UTC integration work well, with position accuracy better than 5.0 m (2σ) and velocity accuracy better than 0.2 m/s (2σ). The UTC BDS/INS integration position/velocity error curves for the level circle trajectory dynamic conditions with maximal acceleration of 100 g and maximal jerk of 10 g/s are shown in Figure 9; the same curves for the vertical circle trajectory are shown in Figure 10.

(2) High dynamic tracking sensitivity test. The tracking sensitivity of the UTC BDS/INS integration was evaluated based on high dynamic profiles with maximal acceleration of 50 g and maximal jerk of 5 g/s, and the results compared with those for the BDS receiver. The test results are shown in Table 5.

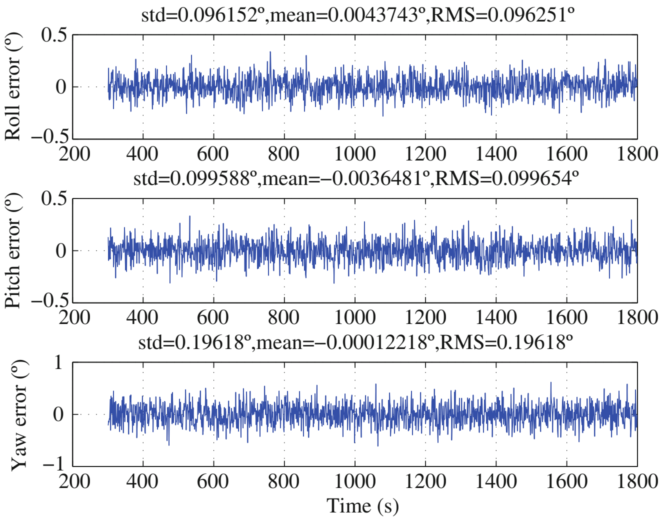

Figure 8 (Color online) Attitude error curve of the UTC BDS/INS integration for 50 g level circle trajectory.

Table 4 The results of position and velocity precision (signal power: −133 dBmW)

	Work mode	Position error (m) (95%)	Velocity error (m/s) (95%)
100 g level circle	BDS receiver	Loss of lock	
	UTC BDS/INS	0.56	0.15
100 g vertical circle	BDS receiver	Loss of lock	
	UTC BDS/INS	1.07	0.19
100 g line-sin	BDS receiver	Loss of lock	
	UTC BDS/INS	0.44	0.18

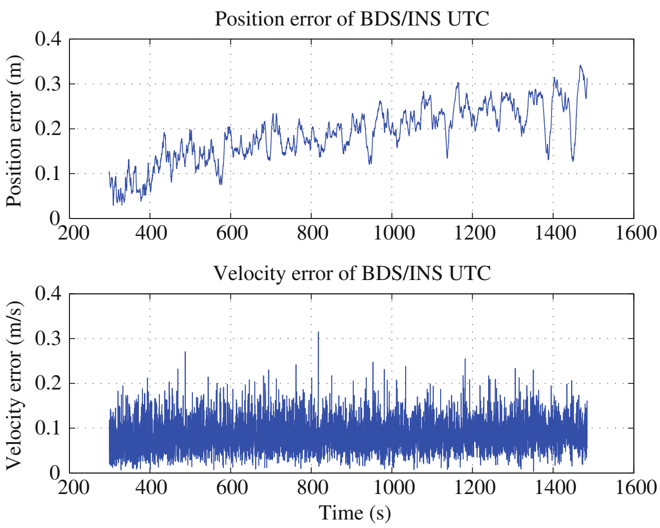

Figure 9 (Color online) Position/velocity error curve of the UTC BDS/INS integration for 100 g level circle trajectory.

Inspection of Table 5 shows that for the conditions of 50 g acceleration and 5 g/s jerk high dynamics, the UTC integration can improve the tracking sensitivity of the BDS receiver by 4–8 dB.

6 Conclusion

The UTC BDS/INS integration improves the overall performance when the BDS receiver operates under weak signal conditions, in dynamic scenarios, and in the presence of jamming. A test system for the UTC BDS/INS integrated navigation system was constructed based on the BDS/INS simulator, and the

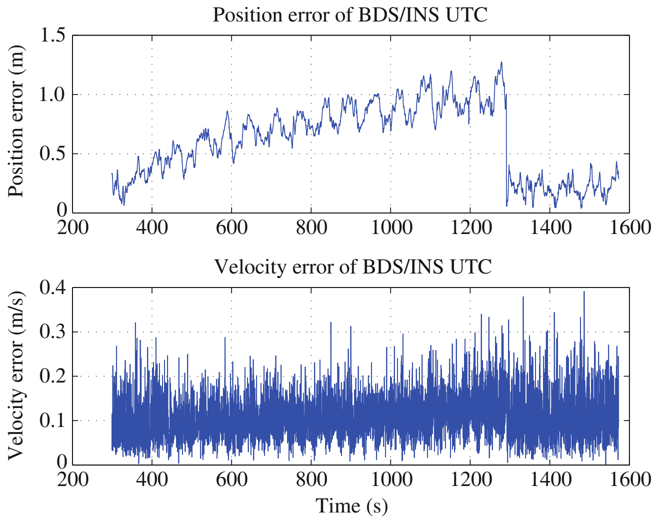

Figure 10 (Color online) Position/velocity error curve of the UTC BDS/INS integration for 100 g vertical circle trajectory.

Table 5 Tracking sensitivity test results

	BDS receiver (dBmW)	UTC BDS/INS integration (dBmW)	Improving sensitivity (dB)
50 g level circle	−133	−141	8
50 g vertical circle	−136	−140	4
50 g line-sine	−134	−141	7

performance was evaluated. Conclusions are drawn as follows.

(1) The UTC BDS/INS integrated navigation system can improve the precision of position and velocity, and also improves the performance of dynamics relative to the high dynamic BDS receiver: 1) For the conditions of 50 g acceleration and 5 g/s jerk high dynamics, the designed high dynamic BDS receiver and the UTC BDS/INS integrated navigation system both work well; however, the UTC integration can improve the precision of position, with position accuracy better than 5.0 m (2σ) and velocity accuracy better than 0.2 m/s (2σ). 2) For the conditions of 100 g acceleration and 10 g/s jerk high dynamics, while the BDS receiver exhibits loss of lock, the UTC integration is accurate with position accuracy better than 5.0 m (2σ) and velocity accuracy better than 0.2 m/s (2σ).

(2) The UTC BDS/INS integrated navigation system can improve the BDS receiver tracking sensitivity relative to the high dynamic performance of the BDS receiver only. For the conditions of 50 g acceleration and 5 g/s jerk high dynamics, the UTC integration can improve the BDS receiver tracking sensitivity by 4–8 dB. Therefore, the UTC integration exhibits an improvement of 4–8 dB compared with that of the designed BDS receiver.

The results of this paper can be applied to high dynamic, strong jamming, and weak signal environments.

Acknowledgements This work was supported by the National Natural Science Foundation of China (Grant No. 61104201).

Conflict of interest The authors declare that they have no conflict of interest.

References

1 Kamel A M M. Context aware high dynamics GNSS-INS for interference mitigation. Dissertation of Doctoral Degree. Calgary: University of Calgray, 2011

2 Paul D G. Principles of GNSS, Inertial, and Multisensor Integrated Navigation Systems. 2nd ed. BOSTON: Artech House, 2013

3 Gao G. INS-assisted high sensitivity GPS receivers for degraded signal navigation. Dissertation of Doctoral Degree. Calgary: University of Calgray, 2007

4 Babu R, Wang J L. Ultra-tight GPS/INS/PL integration: a system concept and performance analysis. GPS Solutions, 2009, 13: 75–82
5 Kreye C, Eissfeller B, Winkel J Ó. Improvements of GNSS receiver performance using ultra-tightly coupled INS measurements. In: Proceedings of the Institute of Navigation GPS/GNSS, Salt Lake City, 2000. 844–854
6 Jorvancevic A, Brown A, Ganguly S, et al. Ultra tightly coupling implementation using real time software receiver. In: Proceeding of the Institute of Navigation GNSS, Portland, 2003. 1575–1586
7 Babu R, Wang J L. Dynamics performnance of carrier and code tracking loops in ultra-tight GPS/JNS/PL integration. In: Proceedings of 2005 Annual IEEE India Conference, Chennai, 2005. 233–236
8 Kim J W, Hwang D H, Sang J L. A deeply coupled GPS/INS integrated Kalman filter design using a linearized correlator output. In: Proceedings of IEEE/ION Position, Location, And Navigation Symposium, San Diego, 2006. 300–305
9 Li D, Wang J L. System design and performance analysis of extended Kalman filter-based ultra-tight GPS/INS integration. In: Proceedings of IEEE/ION Position, Location, And Navigation Symposium, San Diego, 2006. 291–299
10 Babu R, Wang J L. Ultra-tight GPS/INS/PL integration: a system concept and performance analysis. http://www.gmat.unsw.edu.au/snap/publications/babu_etal2005c.pdf/, 2005
11 Spilker J J. Delay-lock tracking of binary signals. IEEE Trans Space Electron Telem, 1963, 9: 1–8
12 Spilker J J. Vector Delay Lock Loop—Position Estimation. United States Patent: No.5398034, 1995
13 Ohlmeyer E J. Analysis of an ultra-tightly coupled GPS/INS system in jamming. In: Proceedings of IEEE/ION Position, Location, and Navigation Symposium, San Diego, 2006. 44–53
14 Buck T M, Wilmot J, Cook M J. A high G, MEMS based, deeply integrated, INS/GPS, guidance, navigation and control flight management unit. In: Proceedings of IEEE/ION Position, Location, and Navigation Symposium, San Diego, 2006. 772–794
15 Soloviev A, Graas F V, Gunawardena S. Implementation of deeply integrated GPS/Low-Cost IMU for reacquistion and tracking of low CNR GPS signals. In: Proceedings of National Technical Meeting, San Diego, 2004. 923–934
16 Soloviev A, Gunawardena S, Graas F V. Deeply integrated GPS/low-cost IMU for low CNR signal processing: flight test results and real time implementation. In: Proceedings of ION GNSS 2004, Long Beach, 2004. 1598–1608
17 Beser J, Alexander S, Crane R, et al. A low-cost guidance/navigation unit integrating a SAASM-based GPS and MEMS IMU in a deeply coupled mechanization. In: Proceedings of ION GNSS 2002, Portland, 2002. 545–555
18 Psiaki M L. Extended Kalman filter methods for tracking weak GPS signals. In: Proceedings of ION GNSS 2002, Portland, 2002. 2539–2553
19 Psiaki M L. Smoother-based GPS signal tracking in a software receiver. In: Proceedings of ION GNSS 2001, Salt Lake City, 2001. 2900–2913
20 Wang H G, Detterich B C. Ultra-Tightly Coupled GPS and Inertial Navigation System for Agile Platforms. United States Patent: No.US20070118286, 2007
21 Yang C. GPS signal tracking with Kalman filter based on joint code delay and carrier phase and frequency error discriminator. In: Proceedings of ION 60th Annual Meeting 2004, Dayton, 2004. 631–640
22 Jee G I, Kim H S, Lee Y J, et al. A GPS C/A code tracking loop based on extented Kalman filter with multipath mitigation. In: Proceedings of ION GNSS 2002. Portland, 2002. 446–451
23 Kim P Y. GPS Navigation with Integrated Phase Track Filter. United States Patent: No.7151486, 2006